

# MHD Instabilities in Current Carrying Heliotron Plasmas

Goshi YAMADA, Yuji NAKAMURA and Katsumi KONDO

*Graduate School of Energy Science, Kyoto University, Uji, Kyoto 611-0011, Japan*

(Received 20 January 2009 / Accepted 21 January 2010)

Instabilities in low beta  $l = 2$  heliotron plasmas with peaked toroidal current density profiles are investigated using resistive reduced magnetohydrodynamic equations. Such heliotron plasmas can have a nonmonotonic rotational transform  $\bar{l}$  profile with two  $\bar{l} = 2/3$  rational surfaces. When the distance between the resonant surfaces is large, resistive instabilities can be found. Current-driven ideal modes with larger growth rates appear when the minimum of the rotational transform becomes just above the rational number  $2/3$  and there is no resonant surface. The existence of this non-resonant mode is explained by the expression for the current-driven term of the plasma potential energy.

© 2010 The Japan Society of Plasma Science and Nuclear Fusion Research

Keywords: heliotron, reduced MHD, resistive mode, current-driven mode, non-resonant mode

DOI: 10.1585/pfr.5.021

## 1. Introduction

In heliotron devices, no net toroidal current is necessary for magnetohydrodynamics (MHD) equilibrium. However, net toroidal currents are observed in experiments in the Large Helical Device (LHD) [1]. Non-inductive currents, such as beam driven and bootstrap currents, are believed to contribute to the observed net currents. It is not clear whether currentless plasmas are more favorable for confinement and whether they are realized in the next generation devices to confine fusion-graded plasma. Therefore, it is worthwhile to investigate heliotron plasmas with toroidal current.

Three different types of flux-averaged current density  $\langle J_{\text{tor}} \rangle$  profile in low beta LHD-like plasma and the corresponding rotational transform  $\bar{l}$  profiles are shown in Fig. 1. In the case of the peaked current density profile, the rotational transform profile becomes a nonmonotonic function due to the large poloidal magnetic field near the center.

MHD instabilities in current-carrying pressureless plasma have been investigated in straight stellarator plasma [2, 3]. They produced stability diagrams with respect to plasma and helical coil currents for kink and tearing modes for various current profiles and helical fields. It was shown later that the stability diagram obtained by calculations including toroidal effect is essentially the same as that given for straight cylindrical plasma [4]. The mode structures of  $m = 1$ ,  $n = 1$  ( $m$  and  $n$  are the poloidal and toroidal mode numbers, respectively) current-driven ideal modes were examined for resonant and non-resonant modes using heliotron E configurations in which the  $\bar{l}$  profile is nonmonotonic and its value at the center is above unity. The plasma displacement of the non-resonant mode was found to have a broad profile in the radial direction, unlike the usual internal kink mode. It is also interesting

to consider localized modes for configurations where the  $\bar{l}$  profile is nonmonotonic and its value at the center is below unity. In such configurations  $m = 1$ ,  $n = 1$  internal kink modes do not appear.

In the present work, we consider low beta LHD-like plasmas with peaked current density profiles in terms of growth rates and eigenfunctions taking account of resistivity. We explore how a resonant localized mode changes as the distance between the rational surfaces becomes small and how non-resonant modes behave when there is no rational surface. Numerical simulations based on reduced resistive magnetohydrodynamic equations are carried out for this purpose.

## 2. Model

The reduced set of magnetohydrodynamic (RMHD) equations for heliotron plasmas [5] is used for the stability analysis. It is based on large aspect ratio ordering. We define  $(x, y, z)$  coordinates as  $x = R - R_c$ ,  $y = Z$ ,  $z = -R_c\varphi$ , where  $(R, \varphi, Z)$  are the cylindrical coordinates and  $R_c$  is the major radius of the plasma center. The time evolution of the system is described by a poloidal flux related to plasma current  $R_c A(x, y, z, t)$ , a stream function  $\phi(x, y, z, t)$ , and plasma pressure  $p(x, y, z, t)$ , where

$$\mathbf{B} = \nabla(\psi_h + A) \times \hat{z} + f_* \hat{z}, \quad (1)$$

and

$$\mathbf{v} = \nabla\phi \times \hat{z}, \quad (2)$$

and  $R_c\psi_h(x, y)$  is a lowest order poloidal flux generated by helical coil current and  $f_*(x, y)$  is a toroidal magnetic field. Here,  $\mathbf{B}$  and  $\mathbf{v}$  represent an effective magnetic field and lowest-order fluid velocity, respectively. Unlike the usual RMHD equations, in which the toroidal magnetic field  $f_*$

author's e-mail: xa52427@pg7.so-net.ne.jp

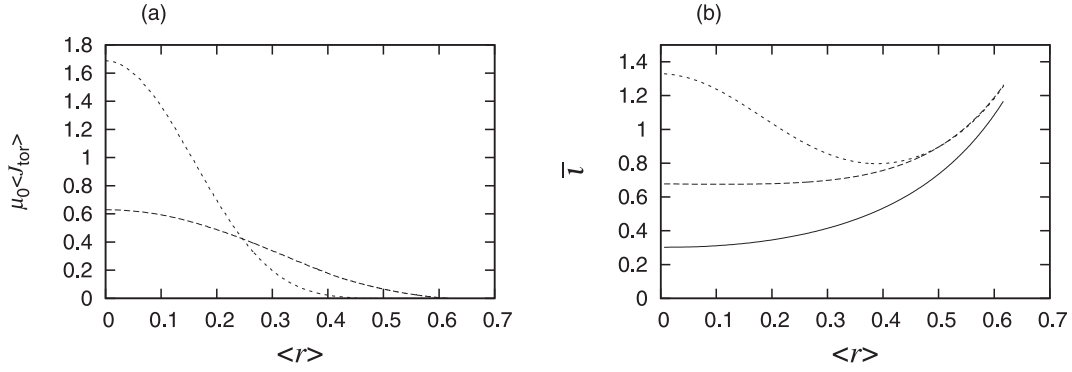


Fig. 1 (a) Averaged current density and (b) rotational transform as a function of averaged minor radius  $\langle r \rangle$  in the low-beta LHD-like configuration. Solid line shows the profile for currentless case. Dashed and dotted lines correspond to the cases of rounded and peaked current density profiles, respectively, with the same total current value.

is uniform in space, we keep  $f_*$  as a flux function to reproduce the same rotational transform profile as in the three dimensional MHD equilibrium.  $A$ ,  $\phi$ , and  $p$  obey the equations

$$\rho_0 \frac{\partial}{\partial t} (\nabla_{\perp}^2 \phi) = \rho_0 [\phi, \nabla_{\perp}^2 \phi] + [\nabla_{\perp}^2 A, A + \psi_h] + f_* \frac{\partial}{\partial z} (\nabla_{\perp}^2 A) + [\Omega, p], \quad (3)$$

$$\frac{\partial A}{\partial t} = [\phi, A + \psi_h] + f_* \frac{\partial \phi}{\partial z} + \eta \nabla_{\perp}^2 A, \quad (4)$$

$$\frac{\partial p}{\partial t} = [\phi, p]. \quad (5)$$

Here, density  $\rho_0$  and resistivity  $\eta$  are assumed to be constant.  $\Omega(x, y)$  represents a potential function of averaged magnetic curvature. The Poisson bracket is defined as  $[f, g] = (\partial f / \partial x)(\partial g / \partial y) - (\partial f / \partial y)(\partial g / \partial x)$ , and the Laplacian as  $\nabla_{\perp}^2 f = \partial^2 f / \partial x^2 + \partial^2 f / \partial y^2$ .

In the present treatment, we consider only the linear development of the system. Linearizing Eqs. (3)-(5) yields the following set of equations for perturbed variables  $\tilde{A}$ ,  $\tilde{\phi}$ , and  $\tilde{p}$ :

$$\rho_0 \frac{\partial}{\partial t} (\nabla_{\perp}^2 \tilde{\phi}) = [\nabla_{\perp}^2 \tilde{A}, \psi_{\text{eq}}] + f_* \frac{\partial}{\partial z} (\nabla_{\perp}^2 \tilde{A}) - [J_{\text{eq}}, \tilde{A}] + [\Omega, \tilde{p}], \quad (6)$$

$$\frac{\partial \tilde{A}}{\partial t} = [\tilde{\phi}, \psi_{\text{eq}}] + f_* \frac{\partial \tilde{\phi}}{\partial z} + \eta \nabla_{\perp}^2 \tilde{A}, \quad (7)$$

$$\frac{\partial \tilde{p}}{\partial t} = [\tilde{\phi}, p_{\text{eq}}], \quad (8)$$

where  $A_{\text{eq}}$  and  $p_{\text{eq}}$  are equilibrium quantities, and  $\psi_{\text{eq}} = A_{\text{eq}} + \psi_h$ ,  $J_{\text{eq}} = -\nabla_{\perp}^2 A_{\text{eq}}$ . Here,  $p_{\text{eq}}$  and  $f_*$  are functions of  $\psi_{\text{eq}}$ . Three-dimensional equilibrium, which is calculated with the VMEC code [6], is toroidally averaged and the resulting two-dimensional equilibrium is used in the linear stability analysis. The averaged equilibrium quantities are calculated as shown in the Appendix.

We apply an  $(r, \theta, \zeta)$  coordinate system for the geometry considered here, where  $r$ , which labels the surface of constant  $\psi_{\text{eq}}$ , is the averaged minor radius, and  $\theta$  and  $\zeta$ ,

which range from 0 to  $2\pi$ , correspond to the poloidal and toroidal angles, respectively. The transformation of variables between the  $(r, \theta, \zeta)$  and  $(x, y, z)$  coordinate systems can be written as

$$x = x(r, \theta), \quad (9)$$

$$y = y(r, \theta), \quad (10)$$

$$z = R_c \zeta. \quad (11)$$

The poloidal angle  $\theta$  is chosen such that the two-dimensional Jacobian,  $\mathcal{J} = (\partial x / \partial r)(\partial y / \partial \theta) - (\partial x / \partial \theta)(\partial y / \partial r)$  is constant on the flux surface. In this case, a straight line  $\theta - \bar{\iota} \zeta = \text{const}$  on the  $\theta$ - $\zeta$  plane becomes a magnetic field line by the transformation of variables, where  $\bar{\iota}$  is the rotational transform. In the  $(r, \theta, \zeta)$  coordinate system, the Poisson bracket is written as

$$[f, g] = \left( \frac{\partial f}{\partial r} \frac{\partial g}{\partial \theta} - \frac{\partial f}{\partial \theta} \frac{\partial g}{\partial r} \right) \mathcal{J}^{-1}, \quad (12)$$

and the Laplacian as

$$\begin{aligned} \nabla_{\perp}^2 f = & \left[ \left( \frac{\partial x}{\partial \theta} \right)^2 + \left( \frac{\partial y}{\partial \theta} \right)^2 \right] \left( -\frac{\partial y}{\partial \theta} \frac{\partial^2 x}{\partial r^2} + \frac{\partial x}{\partial \theta} \frac{\partial^2 y}{\partial r^2} \right) \\ & - 2 \left( \frac{\partial x}{\partial r} \frac{\partial x}{\partial \theta} + \frac{\partial y}{\partial r} \frac{\partial y}{\partial \theta} \right) \left( -\frac{\partial y}{\partial \theta} \frac{\partial^2 x}{\partial r \partial \theta} + \frac{\partial x}{\partial \theta} \frac{\partial^2 y}{\partial r \partial \theta} \right) \\ & + \left[ \left( \frac{\partial x}{\partial r} \right)^2 + \left( \frac{\partial y}{\partial r} \right)^2 \right] \left( -\frac{\partial y}{\partial \theta} \frac{\partial^2 x}{\partial \theta^2} + \frac{\partial x}{\partial \theta} \frac{\partial^2 y}{\partial \theta^2} \right) \mathcal{J}^{-3} \frac{\partial f}{\partial r} \\ & + \left[ \left( \frac{\partial x}{\partial \theta} \right)^2 + \left( \frac{\partial y}{\partial \theta} \right)^2 \right] \left( \frac{\partial y}{\partial r} \frac{\partial^2 x}{\partial r^2} - \frac{\partial x}{\partial r} \frac{\partial^2 y}{\partial r^2} \right) \\ & - 2 \left( \frac{\partial x}{\partial r} \frac{\partial x}{\partial \theta} + \frac{\partial y}{\partial r} \frac{\partial y}{\partial \theta} \right) \left( \frac{\partial y}{\partial r} \frac{\partial^2 x}{\partial r \partial \theta} - \frac{\partial x}{\partial r} \frac{\partial^2 y}{\partial r \partial \theta} \right) \\ & + \left[ \left( \frac{\partial x}{\partial r} \right)^2 + \left( \frac{\partial y}{\partial r} \right)^2 \right] \left( \frac{\partial y}{\partial r} \frac{\partial^2 x}{\partial \theta^2} - \frac{\partial x}{\partial r} \frac{\partial^2 y}{\partial \theta^2} \right) \mathcal{J}^{-3} \frac{\partial f}{\partial \theta} \\ & + \left[ \left( \frac{\partial x}{\partial \theta} \right)^2 + \left( \frac{\partial y}{\partial \theta} \right)^2 \right] \mathcal{J}^{-2} \frac{\partial^2 f}{\partial r^2} \\ & - 2 \left( \frac{\partial x}{\partial r} \frac{\partial x}{\partial \theta} + \frac{\partial y}{\partial r} \frac{\partial y}{\partial \theta} \right) \mathcal{J}^{-2} \frac{\partial^2 f}{\partial r \partial \theta} \\ & + \left[ \left( \frac{\partial x}{\partial r} \right)^2 + \left( \frac{\partial y}{\partial r} \right)^2 \right] \mathcal{J}^{-2} \frac{\partial^2 f}{\partial \theta^2}. \end{aligned} \quad (13)$$

Because the equilibrium studied here has up-down symmetry, perturbed variables can be expanded in Fourier series of the form

$$\tilde{A} = \sum_m A_m(r, t) \sin(m\theta - n\zeta), \quad (14)$$

$$\tilde{\phi} = \sum_m \phi_m(r, t) \cos(m\theta - n\zeta), \quad (15)$$

$$\tilde{p} = \sum_m p_m(r, t) \sin(m\theta - n\zeta), \quad (16)$$

where  $m$  and  $n$  are the poloidal and toroidal mode numbers, respectively.

With the use of finite difference techniques, Eqs. (6)-(8) yield

$$\mathcal{B} \frac{\mathbf{x}^{n+1} - \mathbf{x}^n}{\Delta t} = \mathcal{A} \mathbf{x}^n, \quad (17)$$

where  $\Delta t$  is the time step, and a vector  $\mathbf{x}^n$  represents the values of perturbed quantities at each radial mesh point at the time  $n\Delta t$ . Here,  $\mathcal{A}$  and  $\mathcal{B}$  are coefficient matrices made up of equilibrium quantities. Equation (17) is related to the eigenvalue problem

$$\mathcal{A} \mathbf{p} = \lambda \mathcal{B} \mathbf{p}, \quad (18)$$

where the eigenvalue  $\lambda$ , corresponding to the growth rate, and the eigenvector  $\mathbf{p}$ , which displays the form of the mode that grows with the growth rate  $\lambda$  when Eq. (17) is evolved with time, are to be determined. In the present study,  $\lambda$  and  $\mathbf{p}$  are determined by applying the inverse power method [7]. In this method, the iteration equation

$$(\mathcal{A} - \hat{\lambda} \mathcal{B}) \mathbf{y}_{n+1} = \mathcal{B} \mathbf{y}_n, \quad (19)$$

is used;  $\hat{\lambda}$  is an arbitrarily chosen value. In the limit of  $n \rightarrow \infty$ ,  $\mathbf{y}_n$  is proportional to  $(\lambda_0 - \hat{\lambda})^{-n} \mathbf{p}_0$ , where  $\lambda_0$  is the eigenvalue nearest to  $\hat{\lambda}$ , and  $\mathbf{p}_0$  is the eigenvector associated with  $\lambda_0$ . Making use of this relation, one can evaluate one of the eigenvalues which depends on  $\hat{\lambda}$  and its corresponding eigenvector.

## 3. Numerical Results

### 3.1 Equilibria

The helical coils in the LHD consist of three layers. As the coil current flows inward, the rotational transform becomes higher. In this study, we choose a model configuration with coil current flowing only in the middle layer. Also, the position of the vacuum-field magnetic axis is adjusted to  $R_0 = 3.75$  m. Vacuum magnetic flux surface is calculated by the KMAG code and the obtained last flux surface is used as a fixed boundary in the MHD equilibrium code VMEC. The pressure  $P(s)$  and net toroidal current  $J(s)$  profiles, which are used as input to the VMEC code, are given by

$$P(s) = P_0(1 - s)^2, \quad (20)$$

$$J(s) = J_0[1 - (1 - s)^8], \quad (21)$$

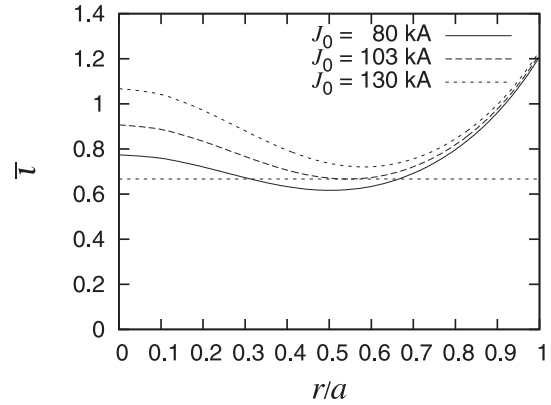


Fig. 2 Rotational transform profiles for various total currents. Horizontal dotted line indicates  $\bar{t} = 2/3$ . The minimum value of  $\bar{t}$  is just  $2/3$  for  $J_0 = 103$  kA.

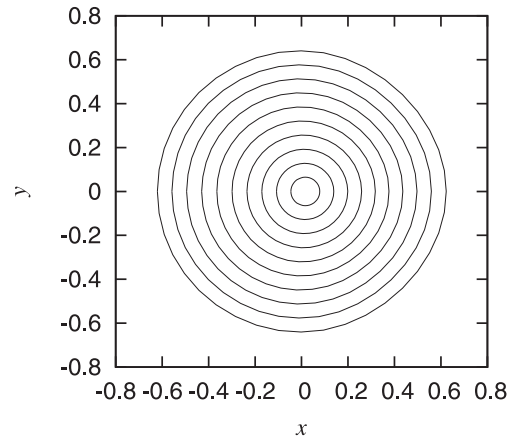


Fig. 3 Contours of poloidal flux for the averaged equilibrium with  $J_0 = 103$  kA.

with  $P_0$  and  $J_0$  constant, where  $s$  is the toroidal flux normalized to its edge value. Note that the current density profile is peaked in the center region. The central magnetic field is  $B_0 = 3$  T, and the beta value at the magnetic axis is  $\beta_0 = 0.2\%$ . The total current  $J_0$  is varied in the range of  $80 \text{ kA} < J_0 < 130 \text{ kA}$ . The corresponding rotational transform profiles  $\bar{t}(r)$  are shown in Fig. 2. Two  $\bar{t} = 2/3$  rational surfaces exist for  $J_0 < 103$  kA, and no  $\bar{t} = 2/3$  surface exists for  $J_0 > 103$  kA. Figure 3 shows surfaces of constant  $\psi_{\text{eq}}$  for  $J_0 = 103$  kA. The averaged flux surfaces are nearly circular, and the magnetic axis is shifted slightly outward from the center of the plasma surface. The averaged radius of the outermost surface is  $a = 0.63$  m. The flux surfaces for the other cases are very similar to this configuration.

### 3.2 Current-driven term

There is a relation for the plasma energy corresponding to the RMHD model, which is expressed as

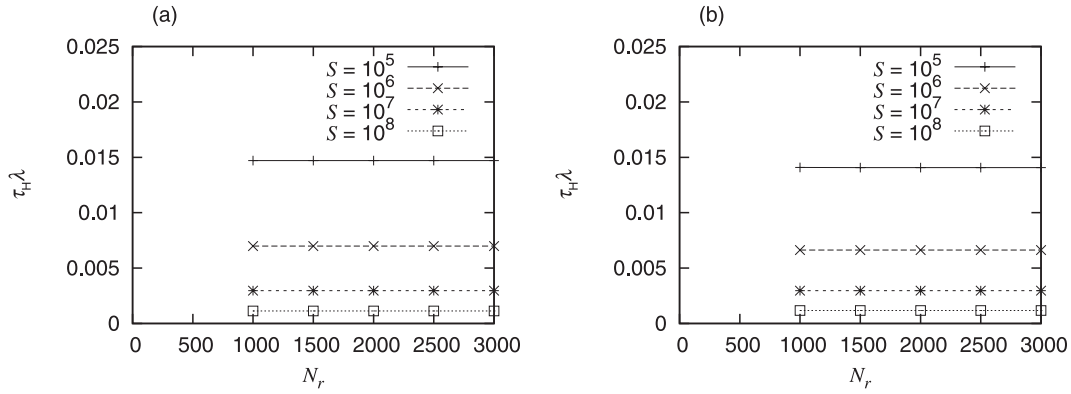


Fig. 4 Numerical convergence of the growth rates with increasing  $N_r$  for (a)  $n = 2$  and (b)  $n = 4$  modes. The results shown correspond to the LHD-like equilibrium with  $J_0 = 83$  kA.

$$-\lambda^2 \rho_0 \int dr |\xi_\perp|^2 = \int dr \left[ |\mathbf{Q}_\perp|^2 - J_{\text{eq}} \mathbf{Q}_\perp \times \xi_\perp \cdot \hat{z} + (\nabla \Omega \cdot \xi_\perp) (\nabla p_{\text{eq}} \cdot \xi_\perp) \right], \quad (22)$$

where  $\lambda$  is the growth rate, and

$$\xi_\perp = \nabla \tilde{\phi} \times \hat{z}, \quad (23)$$

$$\mathbf{Q}_\perp = \nabla \left[ \tilde{\phi}, \psi_{\text{eq}} \right] + f_* \frac{\partial \tilde{\phi}}{\partial z} \times \hat{z}. \quad (24)$$

This equation holds only if the resistivity is zero. The first term on the right-hand side is absolutely positive, whereas the remaining two terms can be negative and thus can drive instability. In the present analysis of low-beta plasma, the first of these, which is referred to as the current-driven term, is more significant. Using integration by parts, this term can be converted into the expression

$$\delta W_c = \int dr \left[ -(\nabla J_{\text{eq}} \cdot \mathbf{Q}_\perp) \tilde{\phi} \right]. \quad (25)$$

In the cylindrical limit, this is written as

$$\delta W_{c|\text{cylinder}} = 2\pi^2 \int_0^a dr \left[ m_0^2 \langle J_{\text{eq}} \rangle' f_* (\bar{l} - n/m_0) \phi_{m_0}^2 \right], \quad (26)$$

where  $m_0$  is the poloidal mode number of the dominant mode, and  $\langle J_{\text{eq}} \rangle$  is the flux-averaged toroidal current. In the usual case of  $\langle J_{\text{eq}} \rangle' < 0$ , the regions where  $\bar{l} < n/m_0$  and  $\bar{l} > n/m_0$  correspond to the stable and unstable regions, respectively. Configurations without resonant surfaces seem to be more unstable because the region where  $\bar{l} \approx n/m_0$  and  $\bar{l} > n/m_0$  is broader.

### 3.3 Convergence study

The code used in this study, in which the inverse power method is applied to solve the eigenvalue problem, can pick up various modes with different growth rates. Here, we examine only modes with the largest growth rates. The instability of the described equilibria is explored

for  $n = 2$  and  $n = 4$  modes, restricting our consideration to modes relevant to  $\bar{l} = 2/3$  rational surfaces.

The results of the convergence study are shown in Fig. 4; the growth rate is plotted as a function of  $N_r$ . Here,  $N_r$  is the number of radial mesh points, and  $S$  is the magnetic Reynolds number defined as  $S = \tau_R / \tau_H$  with  $\tau_R = a^2 / \eta$  and  $\tau_H = \sqrt{\rho_0 R_0^2 / B_0^2}$ . The growth rates are almost independent of the number of mesh points in the range  $1000 \leq N_r \leq 3000$ . As for the eigenfunctions, the mode structures obtained at different values of  $N_r$  greater than 1000 are almost identical for any case. The fixed value used in this paper is  $N_r = 2000$ . This number is sufficient to evaluate growth rates and eigenfunctions. It is also shown to be sufficient to yield accurate results for the other equilibria.

### 3.4 Resistive modes

Figure 5 shows the growth rate of the fastest growing mode as a function of  $S$ . The growth rate is plotted as a function of  $J_0$  in Fig. 6. When  $J_0 = 99$  and 111 kA with  $n = 2$  and  $J_0 = 99$  and 105 kA with  $n = 4$ , the modes are also unstable without resistivity, as expected from Fig. 5. Figure 7 shows the mode structures for  $J_0 = 83$  kA. The eigenfunctions have the form of the resistive interchange mode in the case of  $S = 10^5$ . The stream function is even with respect to the inner resonant point ( $r/a \approx 0.34$ ), and the poloidal flux has a null point there. When  $S$  is increased, the mode structures change to those of the tearing mode. The stream function becomes an odd function, and the null point of the poloidal flux disappears. The stream function is localized on the left side of the inner rational point, which corresponds to the unstable region for the current-driven contribution described in Sec. 3.2, i.e., the region corresponding to  $\delta W_{c|\text{cylinder}} < 0$ , for  $n = 2$ . Concerning the  $S$  dependence of the growth rate, the scaling exponent defined as  $-(\ln \lambda) / (\ln S)'$  is almost equal to one third, which is that of resistive interchange mode [8], at any point.

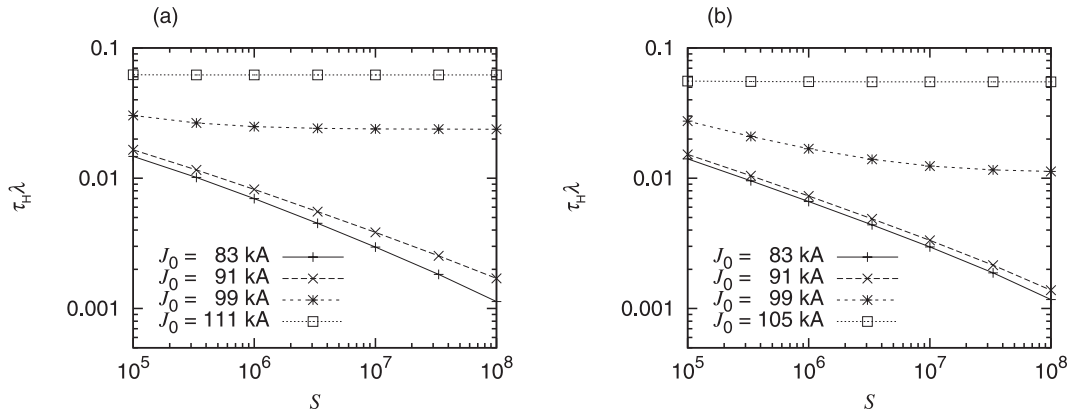


Fig. 5  $S$  dependence of the growth rates of (a)  $n = 2$  and (b)  $n = 4$  modes for various values of  $J_0$ .

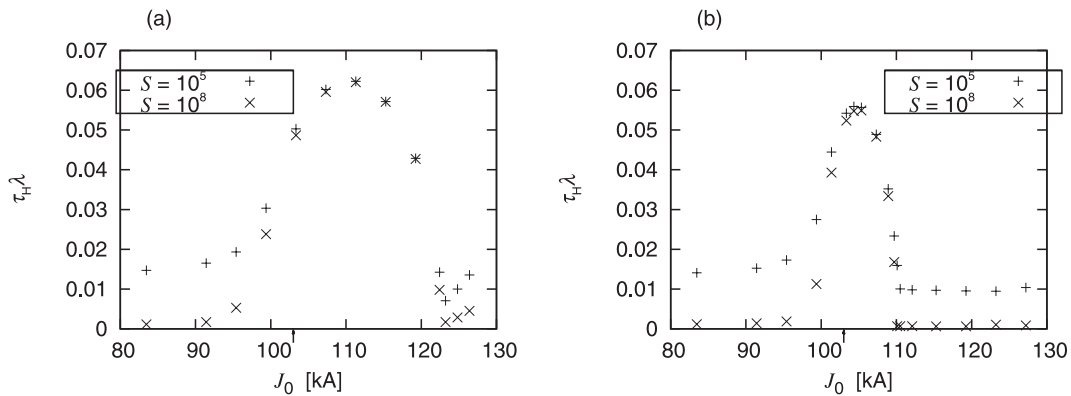


Fig. 6 Growth rate as a function of  $J_0$  of (a)  $n = 2$  and (b)  $n = 4$  modes with  $S = 10^5$  and  $S = 10^8$ . Arrow indicates the point where the minimum value of the rotational transform is  $2/3$ .

### 3.5 Non-resonant modes

Figure 8 shows the mode structures of  $\phi_m$  for  $J_0 = 111$  kA with  $n = 2$  and  $J_0 = 105$  kA with  $n = 4$ . The mode structures change very little for  $S$  ranging from  $10^5$  to  $10^8$ . The stream function is more localized near the point where  $\bar{\iota} = 0$  for  $n = 4$  than for  $n = 2$ . The mode structures are almost identical in the interval where the growth rates of the different values of resistivity in Fig. 6 almost coincide. In this region, the  $\bar{\iota} = 2/3$  rational surfaces disappear, and the modes are non-resonant. The region where these non-resonant modes, which are ideal modes, appear is broader for  $n = 2$  than for  $n = 4$ . When  $J_0$  becomes sufficiently large, the ideal modes are replaced by resistive modes whose dominant Fourier components are  $m = 2$  and  $m = 5$  for  $n = 2$  and  $n = 4$ , respectively.

The non-resonant modes are more unstable than the resonant modes, as shown above. This contrasts with tokamak cases with hollow current density profiles (reversed central shears). Unlike such heliotron plasmas as analyzed above, the current-driven term contributes to stability for non-resonant modes in tokamak plasmas whose current density profiles are hollow. In such tokamak plasmas, the rotational transform is below the relevant rational value, and the toroidal current density has a negative gradient as

a function of radius in the region where the perturbation of a non-resonant mode tends to be localized, i.e., where  $\bar{\iota} \simeq 0$ .

### 3.6 Tokamak cases

For reference, in the following we show the results of ideal stability calculations on cylindrical plasmas of tokamaklike equilibria with hollow current density profiles. This stability analysis is based on the full MHD equations. The linearized ideal MHD [9] is used for more accurate calculation, although the expression for the current-driven term in the ideal MHD model is different from that in the RMHD model. The equation used is

$$\begin{aligned} \lambda^2 \rho_{m,eq} \bar{\mathbf{v}} = & \frac{1}{\mu_0} (\nabla \times \mathbf{B}_{eq}) \times (\nabla \times (\bar{\mathbf{v}} \times \mathbf{B}_{eq})) \\ & + \frac{1}{\mu_0} (\nabla \times \nabla \times (\bar{\mathbf{v}} \times \mathbf{B}_{eq})) \times \mathbf{B}_{eq} \\ & + \nabla (\bar{\mathbf{v}} \cdot \nabla P_{eq} + \gamma P_{eq} \nabla \cdot \bar{\mathbf{v}}). \end{aligned} \quad (27)$$

Here,  $\rho_{m,eq}$ ,  $\mathbf{B}_{eq}$ , and  $P_{eq}$ , which are equilibrium quantities, denote the mass density, magnetic field, and pressure, respectively.  $\gamma$  is the ratio of the specific heats. The growth rate  $\lambda$  and perturbed velocity  $\bar{\mathbf{v}}$  are to be determined. The

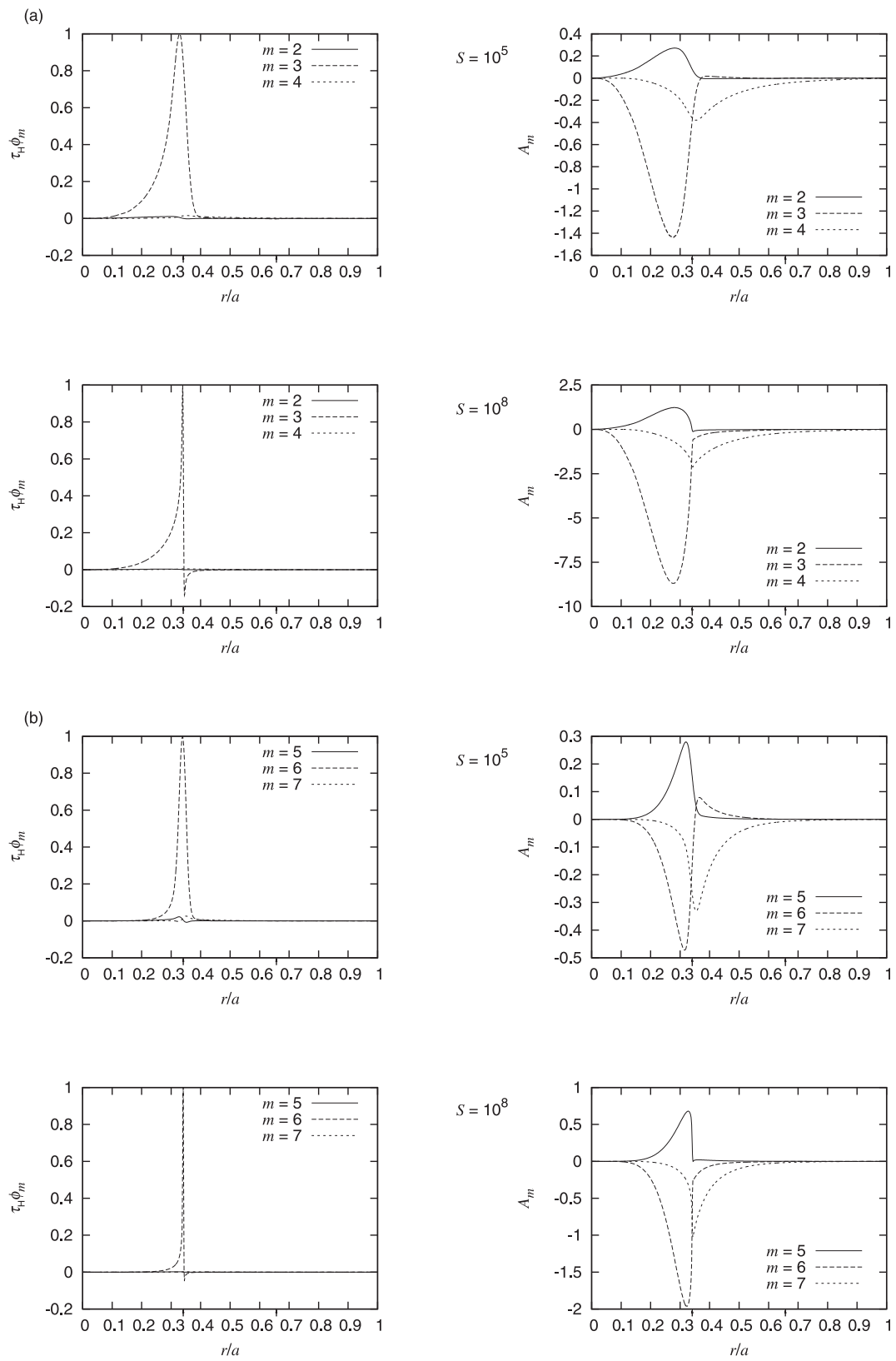


Fig. 7 Eigenfunctions  $\phi_m$  and  $A_m$  for the LHD-like equilibrium with  $J_0 = 83$  kA. The two cases refer to (a)  $n = 2$  and (b)  $n = 4$ . Arrows indicate the positions of  $\bar{\tau} = 2/3$  surfaces.

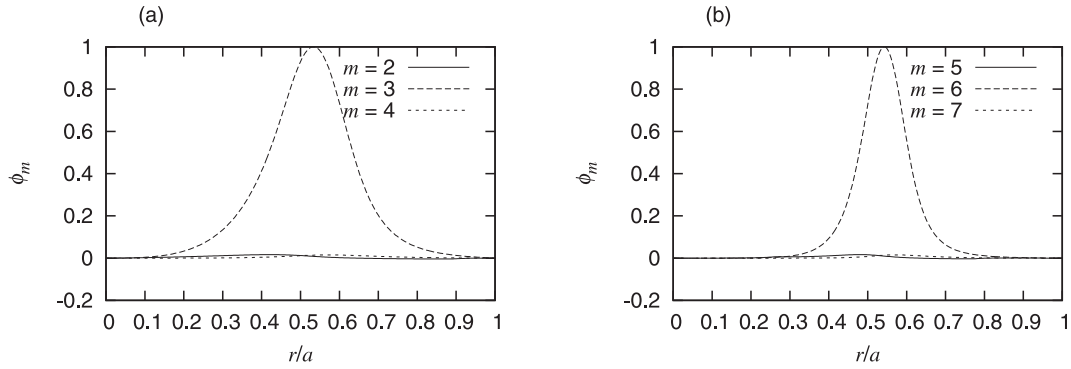


Fig. 8 Eigenfunctions of (a)  $n = 2$  and (b)  $n = 4$  modes for the LHD-like equilibria with (a)  $J_0 = 111$  kA and (b)  $J_0 = 105$  kA. These profiles are obtained at  $S = 10^8$ .

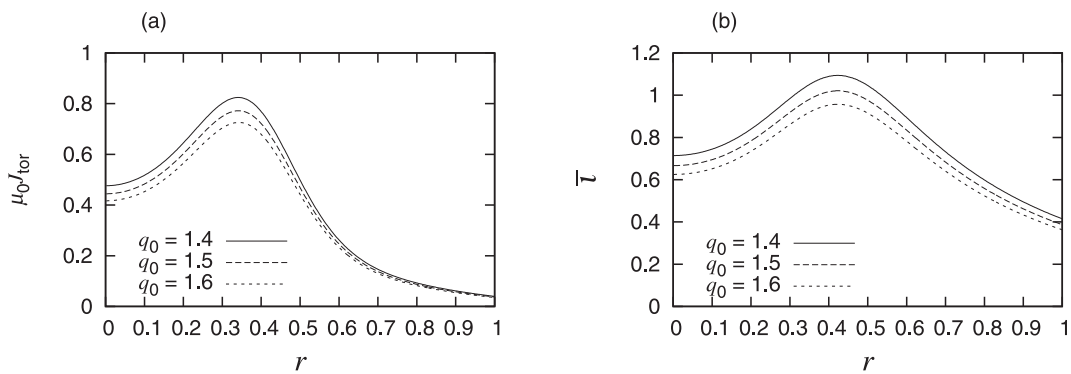


Fig. 9 (a) Toroidal current density and (b) rotational transform as functions of minor radius. Current density profiles are obtained at  $P_0 = 0.05/\mu_0$ . The positions of the peaks in the case of  $P_0 = 0.1/\mu_0$  are much the same as those in this figure.

inverse power method is applied to solve the eigenvalue problem as in the instability analysis for heliotron plasmas. We consider cylindrical plasmas whose pressure and safety factor profiles are given by

$$P(r) = P_0(1 - r^2)^2, \quad (28)$$

$$q(r) = \frac{q_0}{4} \left( 1 + \frac{r^2}{0.412^2} \right) \left( 1 + 3 \exp\left(-\frac{r^2}{0.273^2}\right) \right), \quad (29)$$

with  $P_0$  and  $q_0$  constant. The plasma minor radius and length are 1 m and  $3 \times 2\pi$  m. The central magnetic field is 1 T, and the mass density is assumed to be constant. Also, the poloidal and toroidal mode numbers examined here are  $m = 2$ ,  $n = 2$  because we are concerned with localized modes. Figure 9 shows toroidal current density and rotational transform profiles for various values of  $q_0$ . Note that the peaks of the current density profiles are shifted inward from those of the rotational transform profiles. The growth rate is plotted as a function of the maximum value of the rotational transform  $\bar{\tau}_{\max}$  in Fig. 10 for  $P_0 = 0.05/\mu_0$  and  $0.1/\mu_0$ . It can be seen that the non-resonant modes are more stable than the resonant modes. We now quote the

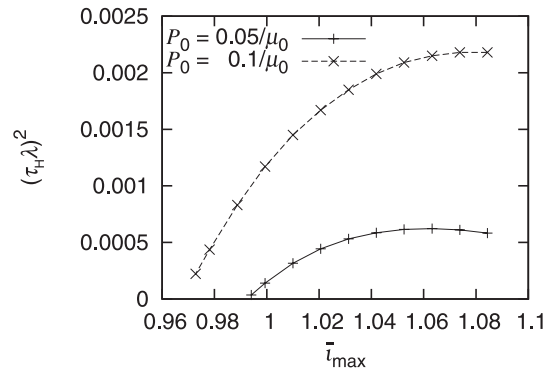


Fig. 10 Growth rates as functions of the maximum value of the rotational transform.  $\tau_H = \sqrt{\mu_0 \rho_0}$  is the Alfvén time with  $\rho_0$  being the constant mass density.

relation for the plasma energy [10],

$$-\lambda^2 K = \delta W_s + \delta W_p + \delta W_c, \quad (30)$$

where  $\delta W_s$  is the sum of all the stabilizing terms, and  $\delta W_p$  and  $\delta W_c$  represent the destabilizing contributions which are referred to as the pressure-driven and current-driven terms, respectively. Also,  $K$  is the kinetic energy. The

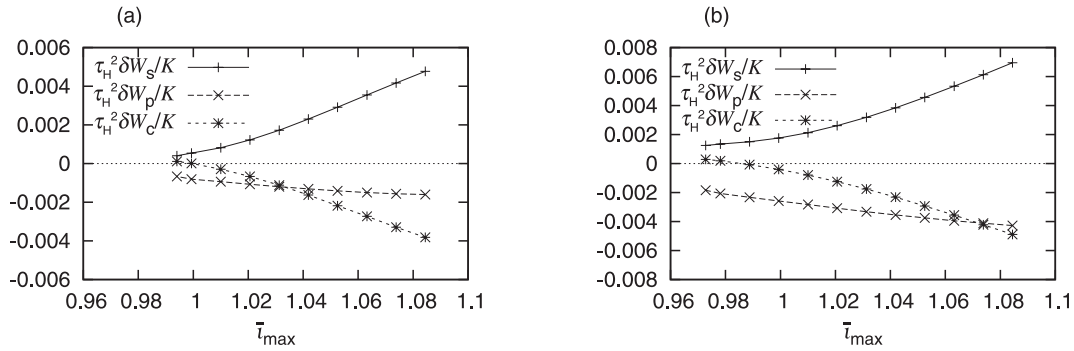


Fig. 11 Potential energies as functions of the maximum value of the rotational transform. The two cases refer to (a)  $P_0 = 0.05/\mu_0$  and (b)  $P_0 = 0.1/\mu_0$ .

values of these potential energies are plotted as functions of  $\bar{\tau}_{\max}$  in Fig. 11. When  $\bar{\tau}_{\max}$  is sufficiently above unity, the contributions of the pressure-driven and current-driven terms are comparable. As  $\bar{\tau}_{\max}$  approaches to unity,  $\delta W_c/K$  becomes small, whereas  $\delta W_p/K$  does not change so much. When  $\bar{\tau}_{\max}$  is below unity, i.e., no resonant surface exists,  $\delta W_c$  makes a stabilizing contribution, as expected from the RMHD model.

## 4. Summary

We investigated instabilities in low beta LHD-like plasmas with peaked toroidal current density profiles using reduced resistive magnetohydrodynamic equations. For relatively small values of total current, the two  $\bar{\tau} = 2/3$  surfaces are separated by a large distance, and resistive modes that have the properties of the resistive interchange mode are found in low  $S$ . The mode structures of the modes change to those of the tearing mode as  $S$  increases. When  $J_0$  is increased such that the separation between the two rational surfaces is small, the system becomes unstable to ideal modes. When  $J_0$  is further increased, current-driven non-resonant global modes with larger growth rates appear. Unlike the case in tokamak plasmas, the current-driven term contributes to instability in the case of a non-resonant mode for such heliotron plasmas as analyzed in this study. This is why the non-resonant modes can be more unstable than the resonant modes.

Kink and tearing modes with  $m = 2$  and  $n = 1$  have been examined previously in configurations of LHD-like plasma similar to the present ones [11]. No unstable non-resonant mode was obtained in those configurations, whereas non-resonant modes appear in the present ones. It is conjectured that  $\langle J_{\text{eq}} \rangle'$  is relatively small in the region where  $\bar{\tau}' \approx 0$  in the previous case and the small current-driven contribution reduces the possibility of instability. There is no pressure-driven contribution to the potential energy due to zero-beta in the case of Ref. [11], and we consider that the zero-beta condition prevents non-resonant modes from becoming unstable. It is pointed out that pressure gradient is not necessary for the instability of non-

resonant modes. In fact, non-resonant modes appear in the zero-beta  $\tau$  calculation with the present configurations corresponding to non-resonance.

## Appendix

The potential function of averaged magnetic curvature is calculated as

$$\Omega(s, \theta_v) = \frac{\langle R^2 \rangle}{R_c^2} - 1 + \frac{\langle R^2 \rangle \langle B_\delta^2 \rangle}{R_c^2 B_c^2}, \quad (\text{A1})$$

where  $R_c$  and  $B_c$  are the major radius and magnetic field at the plasma center, respectively, and  $R$  and  $B_\delta$  are the major radius and oscillating magnetic field component, respectively. Brackets are defined by

$$\langle X \rangle(s, \theta_v) = \int_0^{2\pi} X(s, \theta_v, \zeta_v) d\zeta_v / 2\pi, \quad (\text{A2})$$

for any quantity  $X$ . Here  $(s, \theta_v, \zeta_v)$  are flux coordinates used in the VMEC code,  $s$  labels the flux surfaces, and  $\theta_v$  and  $\zeta_v$  are the poloidal and toroidal angle variables, respectively. The toroidal magnetic field  $f_*$  is given by

$$f_*(s) = -\frac{2\pi R_c \psi'_{\text{eq}}}{\bar{\tau} \int_0^{2\pi} \left( \frac{\partial(R)}{\partial s} \frac{\partial(Z)}{\partial \theta_v} - \frac{\partial(R)}{\partial \theta_v} \frac{\partial(Z)}{\partial s} \right) d\theta_v}, \quad (\text{A3})$$

where  $\psi_{\text{eq}}(s) = (\chi(1) - \chi(s))/R_c$ ;  $2\pi\chi(s)$  is the poloidal flux inside the flux surface labeled by  $s$  in the VMEC code, and  $Z$  is the height above the midplane. The current density  $J_{\text{eq}}(s, \theta_v)$  is determined such that  $J_{\text{eq}} - \Omega dp_{\text{eq}}/d\psi_{\text{eq}}$  is a function only of  $s$ , and the current flowing between the averaged flux surfaces labeled by  $s_1$  and  $s_2$  is equal to that flowing between the flux surfaces labeled by  $s_1$  and  $s_2$  in the VMEC code for any quantities  $s_1$  and  $s_2$ .

- [1] K.Y. Watanabe and LHD Experimental Group, *Proc. 27th EPS Conf. on Controlled Fusion and Plasma Physics, Budapest, Hungary*, **24B** (Institute of Physics Publishing, Bristol, 2000) p. 1316.
- [2] K. Matsuoka, K. Miyamoto, K. Ohasa and M. Wakatani, *Nucl. Fusion* **17**, 1123 (1977).

- [3] M. Wakatani, T. Yoshioka, K. Hanatani, O. Motojima, A. Iiyoshi and K. Uo, *J. Phys. Soc. Jpn.* **47**, 974 (1979).
- [4] T. Matsumoto, Y. Nakamura and M. Wakatani, *Nucl. Fusion* **36**, 1571 (1996).
- [5] H.R. Strauss, *Plasma Phys.* **22**, 733 (1980).
- [6] S.P. Hirshman and J.C. Whitson, *Phys. Fluids* **26**, 3553 (1983).
- [7] L.A. Charlton, J.A. Holmes, H.R. Hicks, V.E. Lynch and B.A. Carreras, *J. Comput. Phys.* **63**, 107 (1986).
- [8] H.P. Furth, J. Killeen and M.N. Rosenbluth, *Phys. Fluids* **6**, 459 (1963).
- [9] J.P. Freidberg, *Ideal Magnetohydrodynamics* (Plenum Press, New York and London, 1987) p.241.
- [10] J.M. Greene and J.L. Johnson, *Plasma Phys.* **10**, 729 (1968).
- [11] K. Ichiguchi, *J. Plasma Fusion Res. SERIES* **5**, 491 (2002).